# Supporting Information

## Smart Porous Wood Supported Flower-like NiS/Ni Conjuction with Vitrimer Co-effect as Multifunctional Material with Reshaping, Shape-memory and Self-healing for High-Performance Supercapacitors, Catalysts and Sensors

Chuanyin Xiong [1]*, Bingbing Li[1], Heguang Liu[2], Wei Zhao[1], Chao Duan[1], Haiwei Wu[1], Yonghao Ni [1,3]

1 Shaanxi University of Science and Technology, Coll Bioresources Chem & Mat Engn, Shaanxi Prov Key Lab Papermaking Technol & Specia, Xi'an 710021, China

2 School of Materials Science and Engineering, Xi'an University of Technology, Xi'an, 710048, China.

3 University of New Brunswick, Limerick Pulp & Paper Ctr, Fredericton, NB E3B 5A3, Canada

* Corresponding author. Tel.:+86 029 88460337; fax: +86 029 88460337.

E-mail address: xiongchuanyin@126.com

The vitrimer is obtained based on the reaction between the bis-cyclic carbonate and tris(2-aminoethy)amine as displayed in Fig. S1 (a). Moreover, compared with thermosetting, thermoplastic material, the vitrimer also possesses chemical cross-links networks as that of thermosetting material, but the networks of vitrimer can be adjusted via thermally-induced exchange reactions between various positions of the polymer chains, without sacrificing the number of bonds and cross-links [1] (Fig. S1 (a)). This unique feature endows the vitrimer with good mechanical properties, remolding, self-healing and shape memory characteristics. Furthermore, the synthesized vitrimer is characterized by infrared spectrum (Fig. S1 (b)). It can be seen from the infrared image that the peak of the double ring changes from 1743cm$^{-1}$ to 1752cm$^{-1}$, which proves that vitrimer is successfully prepared [1]. In addition, some properties of vitrimer are explored by TGA (Fig. S1 (c)). Clearly, the weight loss of vitrimer is only 5% at 212 ℃, which shows that the material has good thermal stability. It can guarantee the capacitor's shape memory and self-healing ability with a wide range of operating temperature. Moreover, the temperature of $T_g$ is 20 ℃ indicating that there is a transition from glass stage to high elastic state at about 20 ℃, which provides a precondition for the shape change of vitrimer. Also, it demonstrates that the vitrimer is a good thermosetting thermoplastic material with certain glass state characteristics and high elastic state characteristics at room temperature.

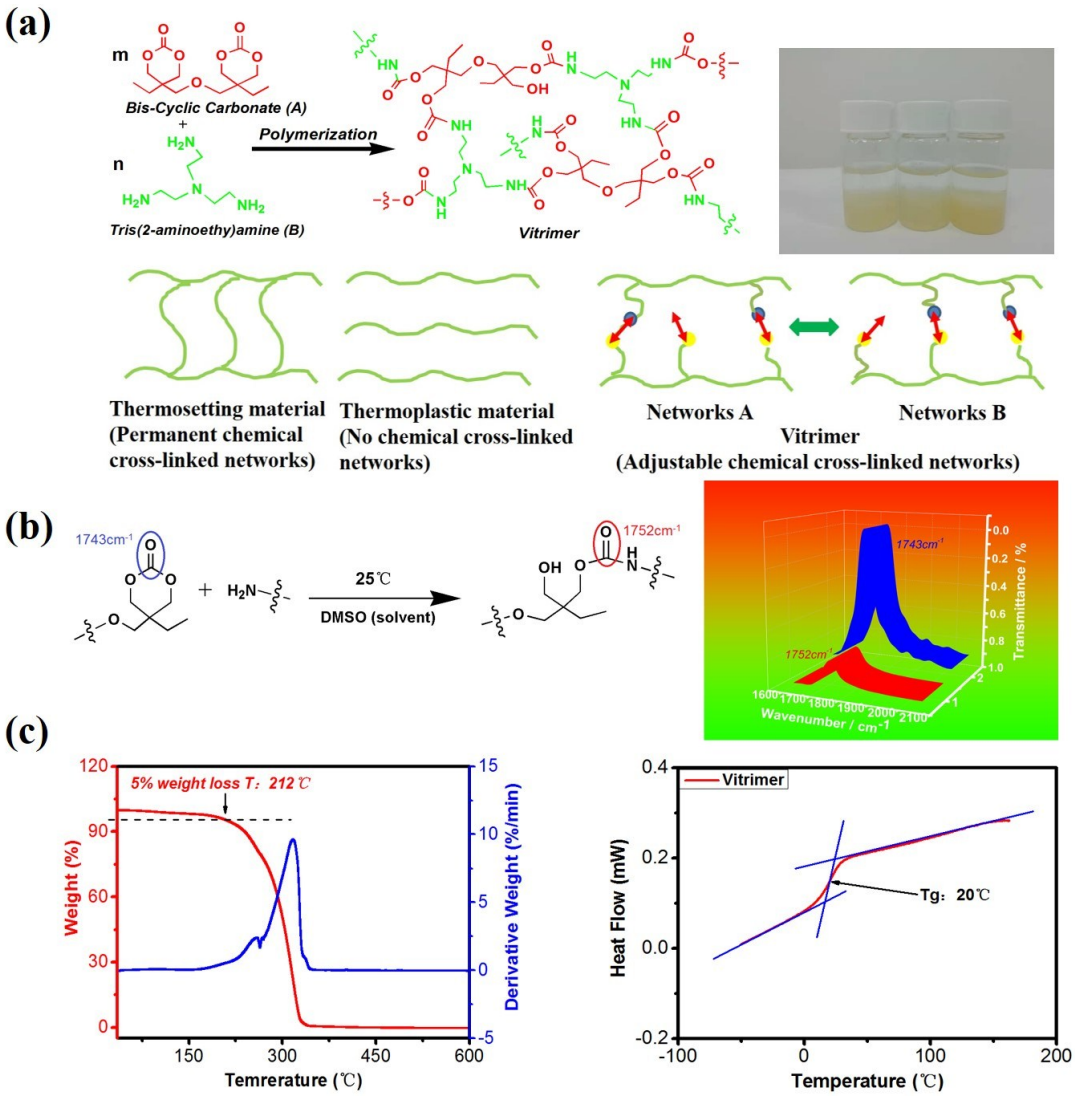


Fig. S1 (a) The specific synthesis route of vitrimer, and differences in molecular topology of thermosetting, thermoplastic and vitrimer material, (b) infrared spectrum and (c) TGA characterization of vitrimer.

The SEM images of CLFW@Ni hybrid under different magnification are presented in Fig. S2, where it can be seen clearly that Ni nanoparticles are densely arranged along the wood tubes, and a 3D connected porous metal network structure is gradually formed due to the confinement effect of the tubes, which is not only conducive to increase the conductivity of the hybrid, but also be beneficial to the transport of electrolyte ions in it.

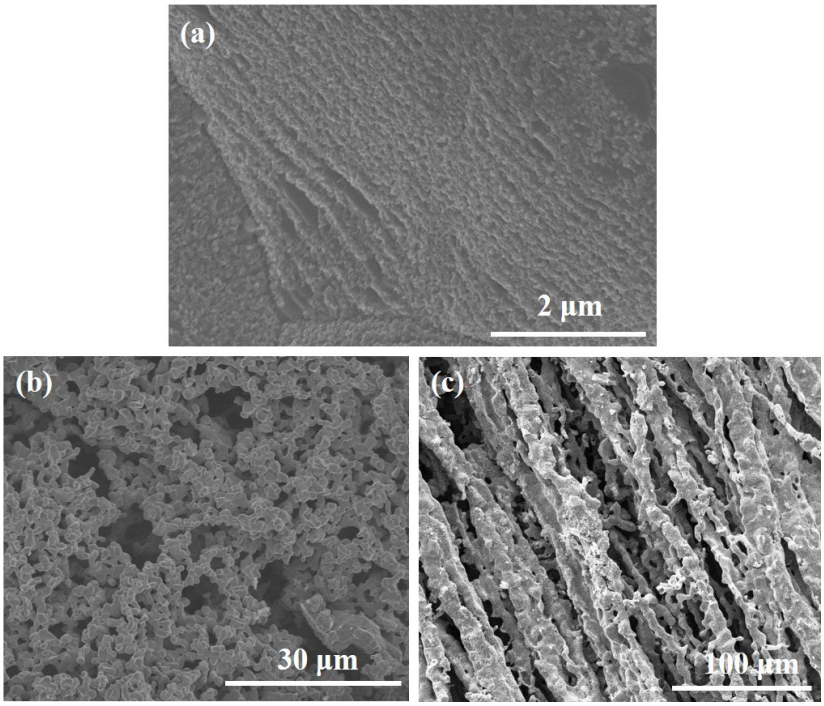


Fig. S2 The SEM morphologies of CLFW@Ni hybrid under different magnification.

The formation of CLFW@Ni-NiS hybrid composed of Ni, C, S, N and O can be further confirmed by elemental mapping images. Fig. S3 (a) shows the overlay image, where it can be observed that the main components of the hybrid are Ni and C. In addition, it can be seen clearly from the Fig. S3 (b-f) that Ni, S and N as the main elements in the hybrid, coming from Ni nanoparticles, NiS and thiourea, respectively are homogeneously dispersed. Besides, there are still a few O elements from wood. Moreover, through the correlation EDS spectra displayed in Fig. S3 (g), it can be further proved that there are five elements in the hybrid including Ni, C, S, N and O, which matches well with the above analysis results.

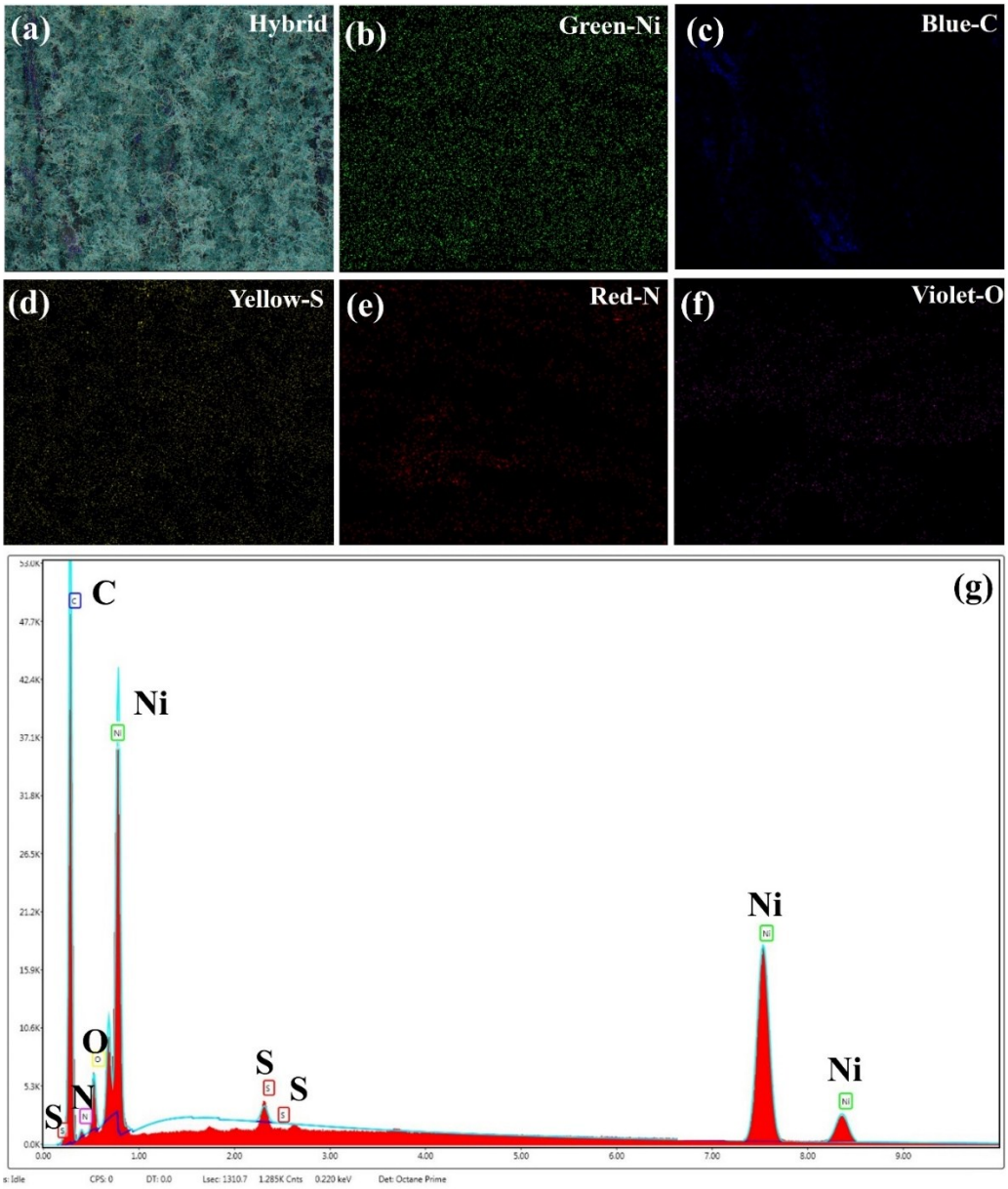


Fig. S3 The EDS images of CLFW@Ni-NiS hybrid with elemental mappings for (a) corresponding overlay image; (b) Ni; (c) C; (d) S; (e) N; (f) O; (g) the EDS of the hybrid.

To check the phase compositions of the above samples after carbonization, the XRD patterns of LFW, CLFW, CLFW@Ni and CLFW@Ni-NiS samples are displayed in Fig. S4 where it can be seen that the characteristic peak at $2\theta = 22.5^\circ$, corresponding to the (002) lattice plane of cellulose [2], disappeared after carbonization instead of a distinct characteristic peak of 26.3 °, corresponding to the (002) crystal plane of graphite carbon [3]. In addition, as a comparison, the XRD pattern of CLFW@Ni

prepared by carbonization of LFW@$NiCl_26H_2O$ is also measured. Apparently, there are two characteristic diffraction peaks at 2θ=44.5 and 51.8 °corresponding to the (111) and (200) planes of Ni, respectively [4, 5] matching well with the above results of TEM, which demonstrates that the Ni nanoparticles are obtained after carbonization (JCPDS 04-0850). Furthermore, for the CLFW@Ni-NiS hybrid, there are two new peaks appeared at 32.20 [6] and 76.2 ° [7], indicating the existence of NiS (JCPDS card No. 10-075-0613 and JCPDS No. 12-0041), which is also consistent with the above result of TEM.

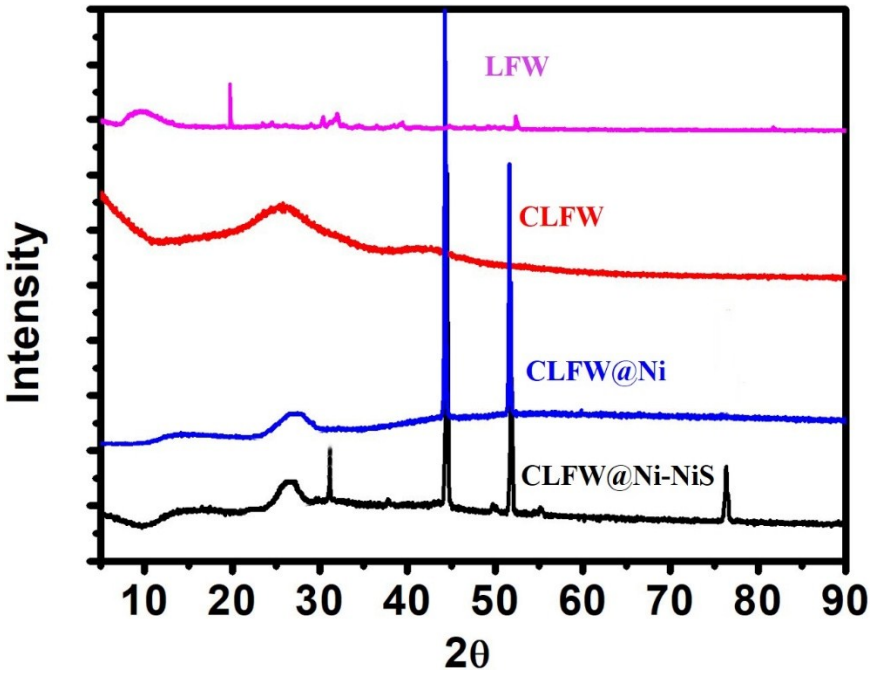


Fig. S4 The XRD patterns of LFW, CLFW, CLFW@Ni and CLFW@Ni-NiS.

In addition, to check the surface chemistry and atomic compositions of the CLFW@Ni-NiS hybrid, XPS is a necessary tool of characterization. Fig. S5 (a) displays the XPS survey spectrum of CLFW@Ni-NiS where the peaks corresponding to C 1s, Ni 2p, S 2p, O 1s and N 1s elemental states are observed. The C 1s spectrum displayed in the Fig. S5 (b) appears a peak at 284.6 eV indicating the presence of $sp^2$-hybridized carbon atoms C=C in CLFW. Additionally, there are another two peaks at 286.1 and 287.7 eV, corresponding to the C−C and C-O bonds, respectively [8]. Furthermore, Fig. S5 (c) presents the Ni 2p spectrum with two major peaks around 856.2 and 873.6 eV, as well as two satellite peaks at 861.4 and 879.6 eV, implying the presence of $Ni^{2+}$ from

the NiS, which matches well with the previous literature [9]. In addition, the peaks are located at the binding energies of 856.2 and 873.6 eV, indicating the existence of metallic Ni in zero valent [9], which is in line with the above XRD and HRTEM results of the CLFW@Ni-NiS hybrid. That is to say, Ni nanoparticles co-exist with the NiS in the CLFW. The S 2p spectrum of the hybrid displayed in Fig. S5 (d) shows two peaks at 161.8 and 163 eV, corresponding to the characteristics of S 2p 3/2 and S 2p 1/2 state of NiS in the hybrid as reported in the previous literature [6]. Additionally, the peaks at 529.7 and 533.1 eV in the O 1s spectrum are ascribed to the C−O and C=O bonds from the CLFW as mentioned above. In addition, the N 1s spectrum shown in the Fig. S5 (f) presents two peaks at around 398.3 and 400.5 eV from thiourea.

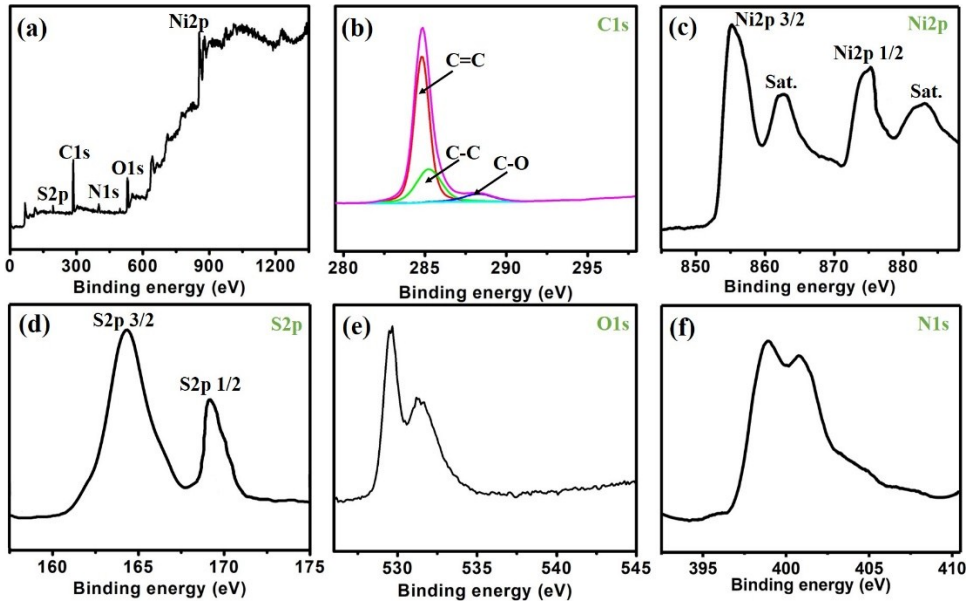


Fig. S5 (a) XPS survey spectrum, and the high resolution spectra of (b) C 1s; (c) Ni 2p; (d) S 2p, (e) O 1s and (f) N 1s elemental states of CLFW@Ni-NiS hybrid.

As a comparison, the thermal stabilities of the LFW, LFW@$NiCl_26H_2O$ and LFW@$NiCl_26H_2O$-Thiourea samples are studied by a TGA in nitrogen over the temperature range of 0−1000 °C as shown in Fig. S6. Obviously, the LFW@$NiCl_26H_2O$ and LFW@$NiCl_26H_2O$-Thiourea samples display a greater degree of weight loss than that of the LFW in the range of 0 to 90 ℃, which is mainly due to the adsorption of a layer of $NiCl_26H_2O$ on the wood surface and pores, so the main water loss is the crystal water of $NiCl_26H_2O$. Furthermore, as the temperature goes further from 90 to 175 ℃,

the LFW and LFW@$NiCl_26H_2O$ samples show almost the same trend, but the LFW@$NiCl_26H_2O$-Thiourea sample still display a greater degree of weight loss, which can be ascribed to the decomposition of thiourea besides the free water and crystal water loss. When the temperature slowly rises from 175 to 360℃， a small amount of the cellulose and hemicellulose in wood begin to decompose, and the decomposition rate becomes violent with the increase of temperature. Furthermore, during the temperature range of 360 to 1000℃, on the one hand, the rest of cellulose, lignin and hemicellulose continue to decompose, meanwhile, the $NiCl_2$ began to decompose to produce Ni nanoparticles, and on the other hand, $NiCl_2$ also react with the $H_2S$ gas generated above to obtain NiS nanofibers with nanoflowers structure under the effect of air flow and wood pipe confinement.

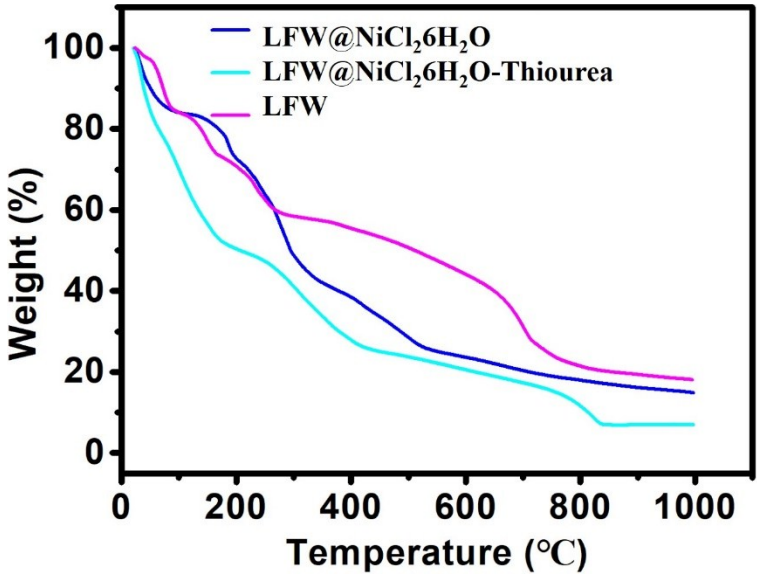


Fig. S6 TGA curves of the LFW, LFW@$NiCl_26H_2O$ and LFW@$NiCl_26H_2O$-Thiourea.

Fig. S7 displays the comparison of the electrochemical performance of the CLFW@Ni-NiS/MIV hybrid electrode in $Li_2SO_4$ aqueous electrolyte and PVA-$H_3PO_4$ solid electrolyte in terms of CV, GCD and AC impedance measurements. As we can see from the Fig. S7 (a, b), compared with the result tested in aqueous electrolyte, the voltage window in solid electrolyte can reach up to approximately 2 V, which helps to increase the energy density of the device. Moreover, the shape of the CV curve still takes on a shape similar to a rectangle, and the GCD curve presents a nearly symmetrical triangle shape in solid electrolyte. Furthermore, the area surrounded by the

CV curve in solid electrolyte shows a bigger value than that of the area in aqueous electrolyte at the same scan rate, meanwhile, the longer discharging time of the hybrid in solid electrolyte is obtained matching well with the comparison results of the CV curves. Additionally, the Nyquist plots of the hybrid in both electrolytes shows almost the same trend, especially in low frequency area, both present a vertical line close to 90 °. All these results indicates that the hybrid has also a good capacitance characteristics in solid electrolyte.

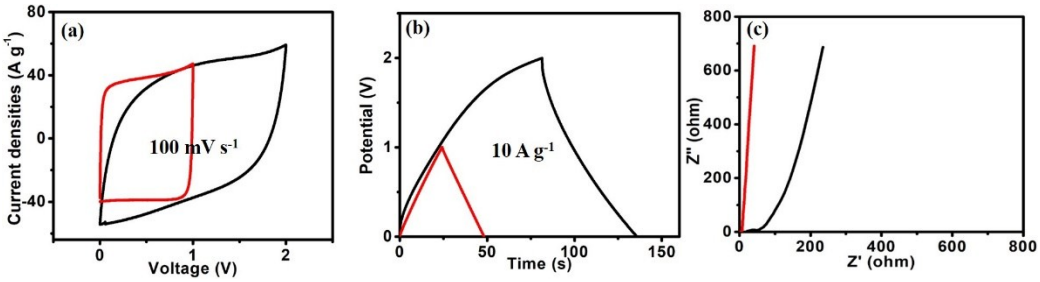


Fig. S7. The comparison of (a) CV curves of the CLFW@Ni-NiS/MIV hybrid electrode at a scan rate of 100 mV $s^{-1}$. (b) GCD curves of the hybrid at a current density of 10 A $g^{-1}$. (c) Nyquist plots of the hybrid in $Li_2SO_4$ aqueous electrolyte and PVA-$H_3PO_4$ solid electrolyte, respectively.

Fig. S8 displays the SEM images of the CLFW@Ni-NiS/MIV hybrid before and after electrochemical testing. It can be observed clearly that there is no obvious change in the microstructure of the CLFW@Ni-NiS/MIV electrode material after 5000 cycles implying a good stability, which matches well with the result of cycle stability of the CLFW@Ni-NiS/MIV hybrid (Fig. 4).

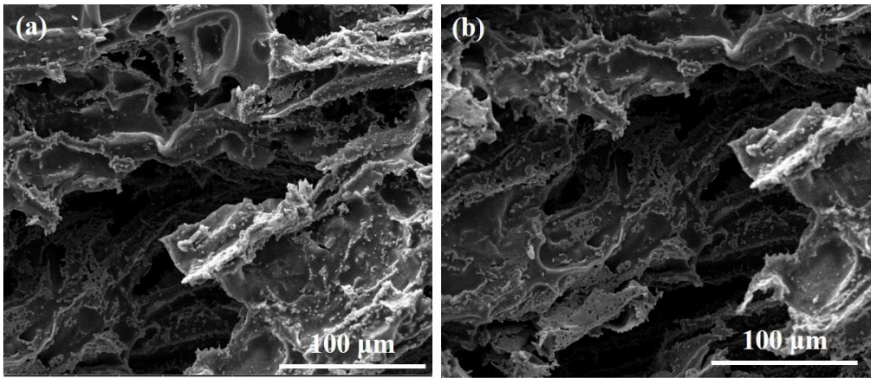


Fig. S8. The SEM images of the CLFW@Ni-NiS/MIV electrode (a) before and (b) after electrochemical testing.

Fig. S9 (a, d, g) presents the CV curves of CLFW, CLFW@Ni-NiS and CLFW@Ni-NiS/MIV electrodes under various scan rates, respectively. Apparently, the CV curves of these electrodes all show nearly rectangle shape regardless of the scan rates, which implies that these hybrid have excellent rate performance. Furthermore, it is found that the current densities of the CLFW@Ni-NiS and CLFW@Ni-NiS/MIV electrodes are much larger than that of CLFW indicating that the specific capacitance is greatly improved. However, the current densities of the CLFW@Ni-NiS and CLFW@Ni-NiS/MIV electrodes basically have no changes, which indicates that the addition of a small amount of vitrimer did not significantly affect the electrochemical properties of the hybrid. Furthermore, the GCD curves for these hybrid at various current densities ranging from 10 to 100 A $g^{-1}$ are shown in Fig. S9 (b, e, h) where it can be observed that the GCD curves are highly linear and symmetrical without obvious voltage drop implying a rapid I–V response, an excellent electrochemical reversibility and little overall resistance. Additionally, under each different current densities, the CLFW@Ni-NiS and CLFW@Ni-NiS/MIV electrodes shows almost the same but much longer discharging time than that of CLFW. All these results are consistent with the results of the CV curves. In addition, through the comparison of the EIS measurements, it is found that all curves exhibit a nearly straight line at a lower frequency region indicating a capacitance characteristics. However, it can be seen clearly by the enlarged images of the EIS measurements that the CLFW@Ni-NiS and CLFW@Ni-NiS/MIV hybrid shows a smaller arc at a higher frequency region than that of the pure CLFW. Moreover, the CLFW@Ni-NiS and CLFW@Ni-NiS/MIV hybrid don't have obvious the 45 ° slope of the Warburg diffusion behavior in the middle frequency region compared with the CLFW electrode (see the insets). As is known to all, the Warburg line represents the frequency dependence of ion diffusion in the electrolyte to the electrode interface. That is to say, the CLFW@Ni-NiS and CLFW@Ni-NiS/MIV hybrid shows an improved capacitance characteristics due to the synergistic effect of natural porous structure of wood, nano porous structure formed by NiS nano flower and

high conductivity of Ni metal nanoparticles, which matches well with the above analysis results.

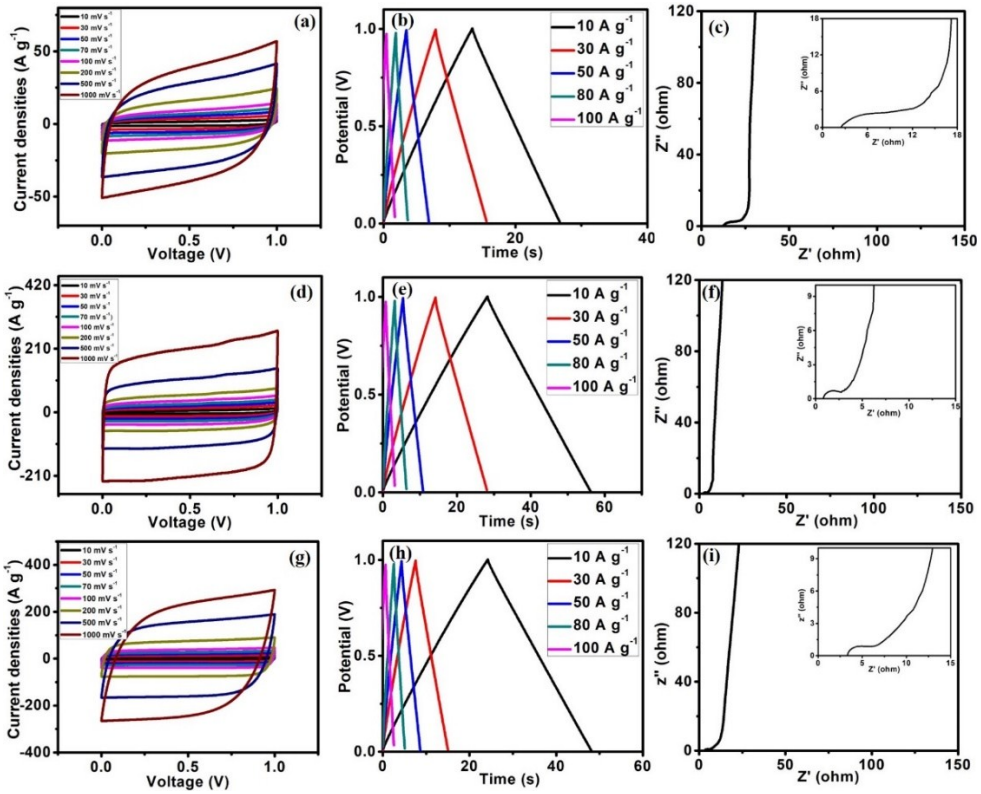


Fig. S9 The CV, GCD curves and EIS measurements of (a) CLFW. (b) CLFW@Ni-NiS. (c) CLFW@Ni-NiS/MIV at various scan rates and current densities ranging from 10 to 1000 mV $s^{-1}$ and 10 to 100 A $g^{-1}$, respectively. The insets located in the Fig. Sx (c, f, i) represent the enlarged regions of the EIS measurements.

Furthermore, the mechanical properties of CLFW, CLFW@Ni-NiS and CLFW@Ni-NiS/MIV are compared (Fig. S10). Apparently, after adding the vitrimer into the hybrid, the CLFW@Ni-NiS/MIV hybrid displays a significantly improved in tensile property than those of the CLFW and CLFW@Ni-NiS.

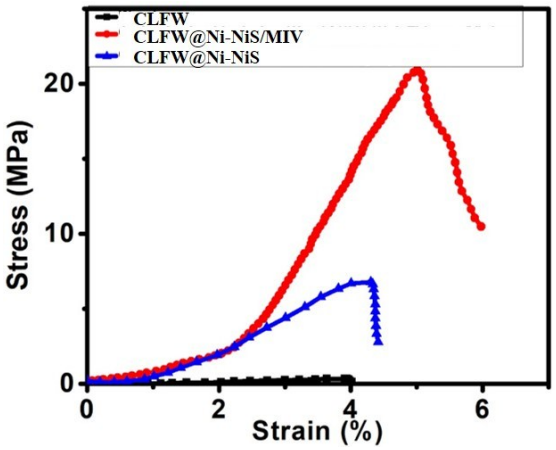


Fig. S10. The comparison of stress-strain curves of CLFW, CLFW@Ni-NiS and CLFW@Ni-NiS/MIV.

It can be seen clearly from the Fig. S11 that as the weight of the weight increases, the bulb becomes brighter and brighter indicating a big increase in current, which is mainly due to the closer contact between Ni nanoparticles as discussed in Fig. 10 (d).

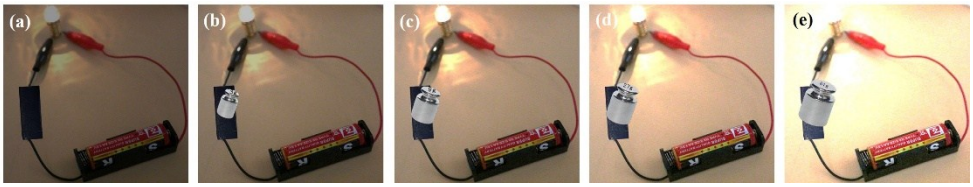


Fig. S11. The change of bulb brightness with the increase of weight. (a) 0 g; (b) 3 g; (c) 9 g; (d) 27 g; (e) 81 g.

Table S1 The electrochemical performance of graphene-based materials from the previous work.

| Hybrid | Electrochemical capacitive characteristic | Ref. |
|---|---|---|
| $Ni_3S_4$@rGO | 37.3 Wh $kg^{-1}$, 0.398 kW $kg^{-}$ | [10] |
| Graphene-$MoS_2$ | 416 F $g^{-1}$ | [11] |
| $MnO_2$@wood carbon | 3600 mF $cm^{-2}$, 1.6 mWh $cm^{-2}$ | [12] |
| SnS/S-Doped Graphene | 642 F $g^{-1}$, 2.98 mF $cm^{-2}$ | [13] |
| 3D porous graphene hydrogel/Aerogels | 196 F $g^{-1}$; 372 mF $cm^{-2}$ | [14] |
| Zn-Ion Hybrid Micro-Supercapacitors | 1297 mF $cm^{-2}$<br>115.4 μWh $cm^{-2}$, 0.16 mW $cm^{-2}$ | [15] |

| | | |
|---|---|---|
| Heteroatom-Doped Porous Carbon Materials | 760 F $cm^{-3}$, 36.8 Wh $L^{-1}$ | [16] |
| Our work | 550 F $g^{-1}$, 5000 mF $cm^{-2}$, 189 F $cm^{-3}$<br>38 Wh $kg^{-1}$, 687 μWh $cm^{-2}$, 58 Wh $L^{-1}$<br>56 kW $kg^{-1}$, 202 mW $cm^{-2}$, 39 kW $L^{-1}$ | — |

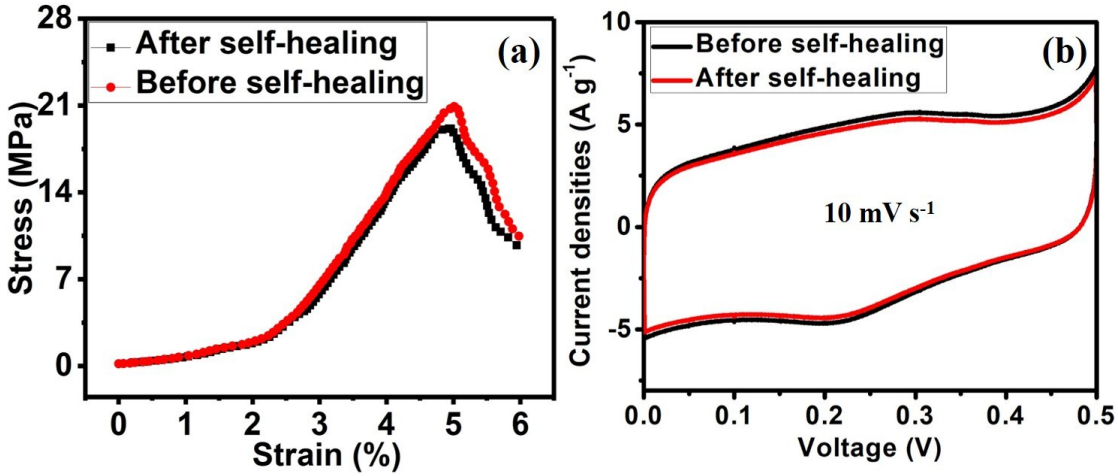


Fig. S12. The comparison of (a) stress-strain curves of CLFW@Ni-NiS/MIV, and (b) CV curves of CLFW@Ni-NiS/MIV before and after self-healing.

**Reference**


[1] W. Zhao, Z. H. Feng, Z. H. Liang, Y. F. Lv, F. K. Xiang, C. Y. Xiong, C. Duan, L. Dai, Y. H. Ni, *ACS Appl. Mater. Interfaces* **2019,** 11, 36090.

[2] Q. F. Zheng, Z. Y. Cai, Z. Q. Ma, S. Q. Gong, *ACS Appl. Mater. Interfaces* **2015,** 7, 3263.

[3] C. Y. Xiong, T. H. Li, A. L. Dang, T. K. Zhao, H. Li, H. Q. Lv, *J. Power Sources* **2016,** 306, 602.

[4] C. Y. Xiong, T. H. Li, T. K. Zhao, Y. D. Shang, A. L. Dang, X. L. Ji, H. Li, J. G. Wang, *Electrochim. Acta* **2016,** 217, 9.

[5] B. K. Urhan, Ü. Demir, *Electrochim. Acta* **2019,** 302, 109-118.

[6] T. C. Ke, B. Vedhanarayanan, L. D. Shao, T. W. Lin, *ChemElectroChem* **2019,** 6, 3806.

[7] N. Parveen, S. A. Ansari, S. G. Ansari, H. Fouad, N. M. Abd El-Salam, M. Hwan Cho, *Electrochim. Acta* **2018,** 268, 82.

[8] Q. Zhang, K. H. Han, S. J. Li, M. Li, J. X. Li, K. Ren, *Nanoscale* **2018,** 10, 2427-2437.

[9] X. D. Yang, M. Zhang, J. Zheng, W. Z. Li, W. J. Gan, J. L. Xu, T. Hayat, N. S. Alharbi, F. Yang, *Appl. Surf. Sci.* **2018,** 439, 128.

[10] Q. Hu, X. F. Zou; Y. H. Huang, Y. Q. Wei, Y. Wang, F. Chen, B. Xiang, Q. B. Wu, W. P. Li, *J. Colloid. Interf. Sci.* **2020,** 559, 115.

[11] A. Gigot, M. Fontana, M. Serrapede, M. Castellino, S. Bianco, M. Armandi, B. Bonelli, C. F. Pirri, E. Tresso, P. Rivolo, *ACS Appl. Mater. Interfaces* 2016, 8, 32842.

[12] C. J. Chen1, Y. Zhang2, Y. J. Li, J. Q. Dai, J. W. Song, Y. G. Yao, Y. H. Gong, I. Kierzewski, J. Xie, L. B. Hu, *Energ. Environ. Sci.* **2017,** 10, 538.

[13] C. Y. Liu, S. L. Zhao, Y. N. Lu, Y. X. Chang, D. D. Xu, Q. Wang, Z. H. Dai, J. C. Bao, M. Han, *Small* **2017,** 13, 1603494.

[14] Y. X. Xu, Z. Y. Lin, X. Q. Huang, Y. Liu, Y. Huang, X. F. Duan, *ACS Nano* 2013, 7, 4042.

[15] P. P. Zhang, Y. Li, G. Wang, F. X. Wang, S. Yang, F. Zhu, X. D. Zhuang, O. G. Schmidt, X. L. Feng, *Adv. Mater.* **2018,** 31, 18016005.

[16] H. L. Jin, X. Feng, J. Li, M. Li, Y. Z. Xia, Y. F. Yuan, C. Yang, B. Dai, Z. Q. Lin, J. C. Wang, J. Lu, S. Wang, *Angew. Chem. Int. Ed.* **2019,** 58, 1.